Real-Time Electron Solvation Induced by Bursts of Laser-Accelerated Protons in Liquid Water

A. Prasselsperger,[1,2] M. Coughlan,[2] N. Breslin,[2] M. Yeung,[2] C. Arthur,[2] H. Donnelly,[2] S. White,[2] M. Afshari,[2] M. Speicher,[1] R. Yang,[1] B. Villagomez-Bernabe,[3] F. J. Currell,[3] J. Schreiber,[1] and B. Dromey[2,*]

[1]*Fakultät für Physik, Ludwig-Maximilians-Universität München, 85748 Garching, Germany*

[2]*Centre for Plasma Physics, School of Mathematics and Physics, Queens University Belfast, Belfast BT7 1NN, United Kingdom*

[3]*The Dalton Cumbria Facility and the School of Chemistry, The University of Manchester, Oxford Rd, Manchester M13 9PL, United Kingdom*

(Received 20 May 2021; accepted 24 September 2021; published 29 October 2021)

Understanding the mechanisms of proton energy deposition in matter and subsequent damage formation is fundamental to radiation science. Here we exploit the picosecond (10^{-12} s) resolution of laser-driven accelerators to track ultrafast solvation dynamics for electrons due to proton radiolysis in liquid water (H_2O). Comparing these results with modeling that assumes initial conditions similar to those found in photolysis reveals that solvation time due to protons is extended by > 20 ps. Supported by magneto-hydrodynamic theory this indicates a highly dynamic phase in the immediate aftermath of the proton interaction that is not accounted for in current models.

DOI: 10.1103/PhysRevLett.127.186001

Ion interactions in matter, and especially in H_2O, are of interest for a wide range of fields including radiation chemistry, medical physics, and technological applications in the nuclear and space industries [1–4]. This is due to a characteristic pronounced energy loss at the end of a well-defined stopping range for ions that permits highly targeted dose delivery. Referred to as the Bragg peak, this behavior is distinct from both lower mass particles (i.e., electrons) and penetrating photons (i.e., x rays) which tend to display a monotonic decay in energy loss with respect to depth. In addition, ions also generate few nm (10^{-9} m) wide tracks of dense ionization ($> 10^{20}$ cm^{-3}) along their trajectories in matter [5,6]. These tracks constitute ultrasteep transverse energy density gradients that seed a rapid, ps-scale evolution of excited electron density. Initially, this evolution tends to homogenize the nanostructured dose distribution and, subsequently, drives the return to equilibrium conditions. However, interrogating the impact of this highly dynamic phase on the radiolytic yields of long-lived ($>$ns, 10^{-9} s) chemically active species and permanent damage site formation in materials irradiated by protons and ions has, to date, been prevented by the limited temporal resolution provided by conventional radio-frequency accelerators ($\sim$100 ps) [7]. This is particularly true for biological relevant studies of chemical species generated by protons and ions interacting in H_2O.

One such species, the solvated electron, is of central importance for understanding radiation chemistry in H_2O. Indeed, its formation remains the focus of much discussion and study [8]. In general, models assume that solvation dynamics due to radiolysis by electrons and ions can be considered to be identical to those measured for photolysis [8–10]. However this assumption remains untested. While ps resolution experiments for laser-driven and ultrafast pulsed electron radiolysis [11–13] have called into question the validity of this equivalence, the absence of absolute timing in those experiments has prevented quantitative analysis for electron interactions [14]. Likewise for proton interactions in H_2O, where irradiation induced dynamics are expected to be more pronounced due to significantly higher energy density, an absence of both ps resolution and absolute timing references have precluded any ultrafast tests of this assumption.

Building on the exciting earlier work for developments towards ultrafast pulsed electron radiolysis [11–14] we find that laser-driven accelerators offer a solution to resolving this problem for ps pulsed ion radiolysis [15]. Recently Dromey *et al.* [16] implemented a real-time optical streak for the investigation of laser accelerated ion bursts in matter. This allows experimental observation of ultra-fast phenomena which could previously only be studied theoretically [17]. Here we capitalize on this technique to investigate electron solvation dynamics in the immediate aftermath of proton irradiation of H_2O with picosecond time resolution. Supported by modeling and a theoretical foundation this provides a detailed picture about solvation yields which can potentially influence the subsequent radiation chemistry. This approach offers a route to establishing a fundamental model for how track structures and their evolution can seed the emerging micro-, and possibly nano-, dosimetry [18].

The experiments were conducted at the *GEMINI* laser facility within the Rutherford Appleton Laboratory.

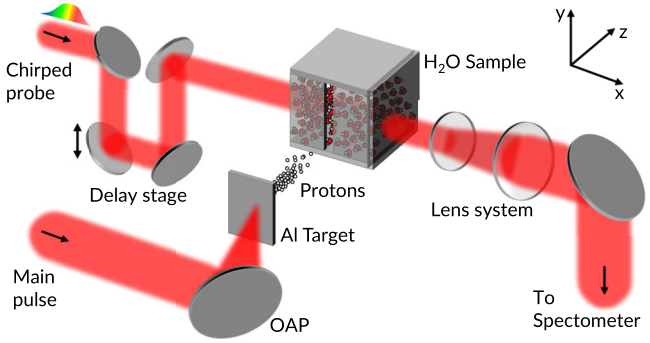

FIG. 1. Scheme of the experimental setting. The main pulse is focused on the target to produce the proton bunch via TNSA. The protons enter the cell trough a Teflon window. The chirped probe pulse propagates through the sample and is then imaged onto the entrance slit of the imaging spectrometer. Each optical streak is then obtained by dividing two back-to-back probe spectra; one with x rays and protons accelerated by the main laser (data shot) interacting in the H_2O pixelwise divided by one without (probe only signal). Depth into the sample is defined in the proton propagation direction (z).

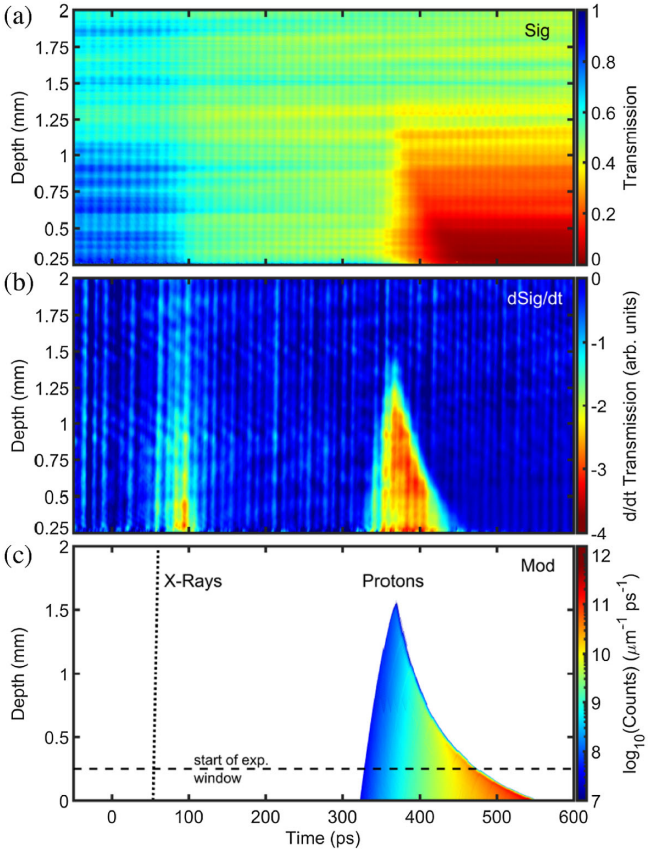

FIG. 2. Observation of proton interaction with time and depth. (a) Optical streak of the samples transmission during x-ray and proton interaction in H_2O (Sig). The maximum incident proton energy was 12.3 ± 0.2 MeV. It should be noted that higher energies were available but given that here we are primarily interested in the stopping dynamics for protons interacting in H_2O energies were chosen to allow this to be studied unambiguously. The interaction of higher energies will be the subject of a future publication. (b) Numerical gradient of (a) (dSig/dt). Here the spatiotemporal distribution of the solvation is revealed. Especially the x-ray signal is observed to stop more than 200 ps prior to protons' arrival. (c) Computational result of secondary electron counts calculated from reproduction of the experimental proton bunch [16,21] (Mod). In each case, the origin of the time axis corresponds to the point of the x rays and protons' emission at the target. Experiments were also performed for which no drop in transmission below noise was observed due to the x-ray burst. Under these conditions the signal due to protons was identical to within uncertainty as Figs. 2(a) and 2(b).

The Ti:sapphire resonators amplify a seed pulse to 15 J. The following compression to a temporal FWHM of 30 fs and focusing down to the minimum spot size yields a maximum intensity of 2×10^{21} W cm^{-2}. The laser is operating at a central wavelength of 800 nm.

In the experiment the main pulse was focused onto a 4 μm thick aluminium foil under a 40° angle to the target normal using a $f/2$ off-axis parabolic mirror (see Fig. 1). As fast electrons are accelerated through the target by the driving laser pulse, an initial burst of prompt x rays generated via bremsstrahlung is emitted. This provides an absolute timing fiducial for the interaction in H_2O (see Fig. 2). Next, the proton burst is generated by the target normal sheath acceleration (TNSA) mechanism. After their initial acceleration, the proton burst drifts to the water cell containing pristine H_2O, with a maximum energy of 12.5 MeV for these experiments [19,20]. A 500 μm collimating slit was used to block the off-axis part of the proton beam. The TNSA protons entered the water cell through a 200 μm Teflon window, implying that incident protons with energy less than 4.3 ± 0.1 MeV were stopped prior to interacting in the H_2O sample.

To visualize the proton interaction in the sample we use a single shot variation of pump-probe technique—single shot optical streaking [16,17,21,22]. In this scheme a probe pulse is split from the main laser pulse. A controllable temporal chirp was introduced to the probe by propagation through a double pass grating setup. For the experiments discussed here, the temporal FWHM was tuned to approximately 1 ns. The synchronization between both the probe and the main pulse enabled the exact adjustment of the relative arrival times at the sample and the target, respectively, by a delay stage. The probe beam passed through the proton-H_2O interaction region transverse to the direction of travel of the TNSA proton bunch. The probe pulse delay was tuned to capture the time frame of the x rays and protons' interaction in the sample. The laser-horizontal axis region (peak proton energy) of the interaction was magnified and imaged on to the entrance slit of a Czerny-Turner spectrometer with a 10 cm × 10 cm, 1200 lines/mm grating. The output from the spectrometer was coupled to a 16-bit CCD camera with 2048 px × 2048 px on

27.6 mm × 27.6 mm to visualize the results. The linear frequency sweep in time of the chirped probe pulse implies that the temporal evolution of the proton interaction is encoded in its spectrum as a reduction in transmission (see below) as it traverses the interaction region. The chosen chirp delivered a temporal resolution of 1.12 ps and the magnification of the probe-beam resolved depth with 4.5 μm per pixel on the CCD.

The drop in transmission of the probe beam is due to a rapid growth in the radiolytic yield of solvated electrons post irradiation. This is a prototypical species in radiation chemistry in H_2O. During the solvation process the electrons oscillate between a quasifree and an excited state with a binding energy of ≈0.26 eV [23]. This initial oscillation relaxes into the solvated state with a binding energy of ≈1.5 eV [24] on a timescale of hundreds of femtoseconds [23,25–29]. The central wavelength of the probe beam at 800 nm corresponds to a photon energy of 1.55 eV. At this energy the solvated electron is still strongly absorbing (∼80% of its maximal value) [27,28,30].

Notably, the time from an ionization event to the solvation of the corresponding electron, i.e., where it becomes detectable in our setting, is on average about 70% to 80% of our temporal resolution.

A typical optical streak is shown in Fig. 2(a). The temporal numerical gradient of Fig. 2(a) is shown in Fig. 2(b). This is important as it allows the dynamic phase of the interaction to be isolated. In Fig. 2(a) the long lived nature of the solvated electron means that the drop in transmission of the probe beam persists for 100 s of ps after the initial interaction which is agreement with nanosecond lifetimes observed in earlier works [12,14]. By obtaining the gradient of this transmission it reveals the temporal window over which the signal in Fig. 2(a) is changing and removes the steady state component of the transient absorption after the initial interaction. Because of interference and diffraction effects the range up to 250 μm was cut in both figures.

Two main features are visible in the data, one starting at 53 ps the other one at 326 ps. The first signal corresponds to the prompt x rays [31]. The second feature at 326 ps is caused by the proton burst. For our experimental parameters the TNSA bunches have been shown to be few ps in duration following drift to the sample under investigation [16]. Considering this, and that the temporal resolution of our detection system is 1.12 ps, proton energies > 4 MeV can be considered to be emitted simultaneously with the prompt x-ray burst [32]. Thus the maximum proton energy can be estimated by their time of flight. For the given data this results in a maximum proton energy of 12.3 MeV. An error of ±0.2 MeV arises from the uncertainty of ±50 μm in detecting the front surface of the sample. This estimate is also corroborated by the stopping range observed for the maximum proton energy in the sample (≈1.5 mm, Fig. 2).

It is important at this point to recognize the significance of two key aspects of this experiment that allow for our high accuracy measurements. First, the prompt x-ray pulse provides absolute timing for the experiment, within the uncertainty to which one can measure the source to sample distance. An error of ±0.3 ps arises, which correlates to one pixel in time. From this all depths and relative times of arrival of the subsequent TNSA proton bunch can be confirmed. Therefore overall uncertainty in the experimental measurement is reduced to noise fluctuations. It is also clear from Fig. 2(b) that all dynamics due to the interaction of the x-ray pulse have stopped more than 200 ps prior to the arrival of the proton bunch. Second, the high instantaneous flux of protons of ≈100 μm^{-2} in 0.5 MeV bandwidth allows the observation of a strong transient absorption signal due to solvated electron generation without the need for scavaging agents [16,21]. This means that using this technique the proton interaction occurs in pristine H_2O.

In Fig. 2(c) the simulated proton interaction is shown. The x-ray pathway is indicated by the vertical dotted line, the horizontal dashed line shows the start of the experimental window. The color map denotes the number of ionized electrons per unit time and depth. The highest considered proton energy was 12.5 MeV to reproduce experimental conditions.

It is important to interpret the spatiotemporal profile for the broadband TNSA bunch stopping in H_2O. The leading edge of the signal with depth corresponds to the propagation path of the highest energy protons in the sample. Energy deposition leads to a deceleration, resulting in a stopping of these protons at approximately 1.5 mm. With elapsing time lower energy protons arrive at the front surface of the sample, showing lower penetration depths, returning the characteristic "shark tooth" profile for the spatiotemporal stopping observed in Fig. 2(b) and 2(c).

To quantitatively calculate the cumulative solvated electron concentration $c_{e_{\mathrm{sol}}}$ from the ionization rates, the following equation was applied:

$$c_{e_{\mathrm{sol}}} \propto \int_{dt}\int_{dV}\int_{dE} \mu_{e_{\mathrm{sol}}} v_e S_{\mathrm{ion}} \frac{d\Psi_p}{dE}\, dE dV dt. \qquad (1)$$

Here, the integrated proton flux spectrum $d\Psi_p/dE$ weighted with the ionization stopping power S_{ion} is proportional to the local ionization rate per unit volume V. The normalized distribution v_e accounts for the part of the temporally and spatially varying electron spectrum that potentially could get solvated. Lastly, $\mu_{e_{\mathrm{sol}}}$ describes the solvation yield which is in competition with other decay mechanisms and strongly depends on the local density of ions, electrons, and hydronium radicals ($H_3O.$). Svoboda *et al.* [8] confirmed that the latter acts as a precursor species of the solvated electron. Precisely, the hydrated $H_3O.$ will spontaneously decay into H_3O^+ and e^- and thus create a

gate for the electron to escape its parenting ion and solvate in the bulk medium [33–35].

Linking this result to the Beer-Lambert law, allows the transmission η to be calculated contingent upon the absorbent concentration via $\log_{10}(\eta) = -\epsilon c_{e_{\mathrm{sol}}} l$. Experimental values of the molar absorptivity ϵ are given by Kimura *et al.* [27], while l relates to the samples dimensions.

Accordingly, transmission along the path of protons of a given initial energy can be derived. Here two effects superimpose. The ionization stopping power increases with depth to the Bragg region. On the other hand the flux decreases due to the protons dissipating both temporally and spatially as successively lower energies stop in the medium. These two effects act in opposition on the radiolytic yield of solvated electrons and, consequently, the overall decrease in transmission with depth is quite low. To quantitatively characterize the processes triggered by the stopping proton bunch according to Eq. (1), the local electron spectra and H_3O species densities related to v_e and $\mu_{e_{\mathrm{sol}}}$, respectively, have to be determined.

Therefore, to obtain a complete picture of the temporal evolution of the different molecular, atomic, and electronic species in the sample during the protons' interaction particle dynamics simulations were performed. This allowed us to determine the expected phase space of a volume within the sample centred at 0.5 mm depth. A time dependent energy spectrum of the ionized electrons within the volume was generated to receive a measure for v_e [see Eq. (1)]. The emergence and decay dynamics of all particles were tracked by numerical integration of rate equations and therewith $\mu_{e_{\mathrm{sol}}}$ [see Eq. (1)] was approximated. The excited solvation state was introduced according to Svoboda *et al.* [8]. Based on the density of solvated electrons the probes transmission was computed.

In Fig. 3 the result is plotted against the corresponding lineout of the experiment. Comparing the overall reduction in transmission shows that experimental and modeled concentrations of solvated electrons are in good agreement with each other. However, there is a delayed decline in the experimentally observed dynamics in comparison to that expected from modeling. The time taken for the signal to drop to its $1/e$ value in the experiment is approximately 22 ps longer than that calculated in the simulation. This suggests that the solvation process is progressively delayed.

We find that the temporal discrepancy between the model and the experiment is rooted in the underlying physics based on ultrafast solvation assumed in the model. From magnetohydrodynamics the macroscopic force acting on a certain density n_α of charged particles α can be derived. The movement is described by the center-of-mass velocity $\mathbf{u}_\alpha$ as

$$m_\alpha\left(\frac{d(n_\alpha \mathbf{u}_\alpha)}{dt} - \frac{d\mathbf{\Gamma}_\alpha}{dt}\right) = q_\alpha n_\alpha(\mathbf{D} + \mathbf{u}_\alpha \times \mathbf{H}) - 3n_\alpha \nabla k T_\alpha + \mathbf{R}_{\alpha\beta}. \quad (2)$$

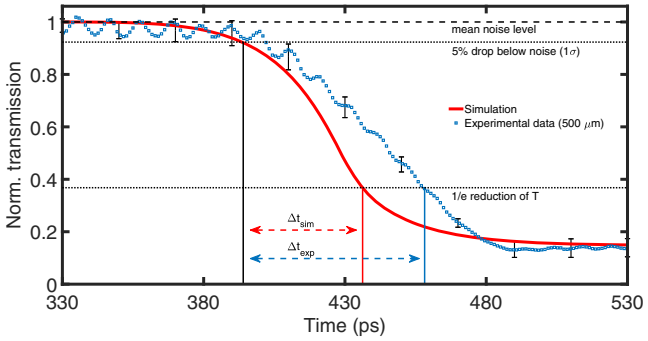

FIG. 3. Opacity caused by solvated electrons. Shown is the mean signal of Fig. 2(a) at 500 ± 50 μm benchmarked against the transmission caused by the calculated solvation yield. The computation was done for the proton bunch given in Fig. 2(c). Both lineouts were normalized to 1. The delay of the experimental signal drop with respect to the simulation can be seen by $\Delta t_{\mathrm{exp}} - \Delta t_{\mathrm{sim}} = 22 \pm 1$ ps.

Here m and q are the particles mass and charge, respectively. The left-hand side of this equation describes the plasma's center-of-mass movement, i.e., applicable for free electrons, protons, and radicals, including its variation by a change in the mass flux $\mathbf{\Gamma}$ due to emerging or decaying particles. The right-hand side combines the distinct forces exerted to drive this movement. Here the first term describes the macroscopic field effects $\mathbf{D}$ and $\mathbf{H}$, respecting also the polarization and magnetization of the H_2O molecules, respectively. The second term contains spatial temperature variations, i.e., the thermal energy kT_α drift. The last term $\mathbf{R}_{\alpha\beta}$ characterizes collisions between the particles and other species β which results in macroscopic friction. With this approach the charge concentrations should be revealed in future studies to precisely determine the local solvation yield $\mu_{e_{\mathrm{sol}}}$ [see Eq. (1)].

As real-time observation of solvated electron formation post-proton irradiation was not available prior to the methodology presented here, the majority of data about solvation came from photolysis experiments. Only the friction term $\mathbf{R}_{\alpha\beta}$ in Eq. (2) can be assumed to be equivalent post proton and photon irradiation as it is dominated by collisions with H_2O molecules. Differences arise with reference to the other terms.

First, the incident protons create a nanometer-scale charge reservoir in the Bragg region as they stop. Here they create a nonequilibrium condition by violating the initial charge neutrality of the sample. Macroscopic fields build up, which corresponds to the $\mathbf{D} + \mathbf{u}_\alpha \times \mathbf{H}$ term. The latter will influence the drift especially of H_3O^+ ions and electrons contrarily and thus decelerate the solvation yield by separating both species. Additionally, it will be highest close to the Bragg region where the charge surplus assembles, which agrees with the observation in Fig. 3.

Second, the transferred energy by the long-ranging Coulomb force raises the average particle energy within

the proton tracks drastically. This is best described by the thermal spike model [36]. The temperature increase ΔT in time t and with distance r from the track can be approximated by [37]

$$\Delta T(r,t) = \frac{\gamma S}{\pi \rho c a^2(t)} e^{-[r^2/a^2(t)]}. \quad (3)$$

Here, γS is the deposited energy in thermal spikes and ρ and c are density and heat capacity of H_2O, respectively. The time dependent factor $a(t)$ describes the dissolution of the spikes. In H_2O maximum temperature increases of $\Delta T_{\max} \approx 200$ K were measured in the Bragg regime of protons [36]. The temperature gradient generates a lower density around the tracks which reduces the solvation rate [see Eq. (2)]. Further, during the thermal relaxation of the excited solvated state into the ground state, its absorption spectrum shifts from the infrared to the equilibrium peaked at 721 nm [24]. The upper levels absorptivity of 800 nm photons is 2.8 times lower [27]. This blueshift takes hundreds of femtoseconds at 300 K [8,23,28,29], however, increases to picoseconds at the increased temperatures [24]. Thus absorption gradually delays with increasing temperature.

Both of these effects predominantly drive the charge mobility and, accordingly, the solvation yield $\mu_{e_{\mathrm{sol}}}$. This could explain the observed temporal delay of more than 22 ps between the simulation and the experiment. It is important to note that during the ultrafast timescale observed here the different species occupy distinct kinetic energy spectra that may not be described in full by the thermal spike model. Despite this, the clear conclusion can be drawn that the processes underlying electron solvation in the aftermath of the passage of protons are significantly different to those following irradiation with ionizing photons.

In summary, we provide direct experimental evidence of ultra-fast electron solvation occurring in the immediate aftermath of proton irradiation of H_2O. The combination of this real-time observation with modeling revealed a solvation process decelerated by as much as 22 ± 1 ps. These results indicate that the dynamics following proton irradiation deviate significantly from the known picture about the solvated state. The underlying physics hints at plasma movements caused by macroscopic fields and temperature spikes to be responsible for this discrepancy.

Here solutions for the fundamental force terms [see Eq. (2)], enabled by real-time optical streaking, provide the basis for a robust framework upon which to build predictive models for a wide range of conditions. Considering the rapid development of laser-driven proton sources [15,38,39] and beam transport [40,41] realizing novel applications in space science [42], radiotherapy [43,44], and industry [45] will hinge on the development of new models. We expect this work to contribute to a deeper understanding of the ultrafast processes underpinning these interactions.

The authors acknowledge support by DFG via project GRK2274 and the cluster of excellence Munich Centre for Advanced Photonics. The authors also would like to acknowledge support from EPSRC Grants No. EP/P010059/1 and No. EP/P016960/1. The experiments were planned and conducted by M. C., N. B., M. Y., C. A., H. D., S. W., M. S., R. Y., F. J. C., J. S., and B. D. Data were analyzed by A. P., M. C., M. A., and B. V.-B. A. P. performed all the calculations with advice from M. C., M. A., B. V.-B., M. Y., J. S., and B. D. The draft of the Letter was written by A. P. with special support by J. S. and B. D. Improvements followed through contributions from all authors. Collaboration between the Ludwig-Maximilians-Universität München and the Queen's University of Belfast was made possible by ERASMUS+. A. P. also wants to gratefully thank J. S. and B. D. for the support during the research project.

*Corresponding author.
b.dromey@qub.ac.uk

[1] J. M. Herbert and M. P. Coons, The hydrated electron, Annu. Rev. Phys. Chem. **68**, 447 (2017).
[2] J. M. Schippers and A. J. Lomax, Emerging technologies in proton therapy, Acta Oncologica **50**, 838 (2011).
[3] W. D. Newhauser and R. Zhang, The physics of proton therapy, Phys. Med. Biol. **60**, R155 (2015).
[4] M. Prall, M. Durante1, T. Berger, B. Przybyla, C. Graeff, P. M. Lang, C. LaTessa, L. Shestov, P. Simoniello, C. Danly, F. Mariam, F. Merrill, P. Nedrow, C. Wilde, and D. Varentsov, High-energy proton imaging for biomedical applications, Nature (London) **6**, 27651 (2016).
[5] M. A. Quinto, J. M. Monti, P. F. Weck, O. A. Fojon, J. Hanssen, R. D. Rivarola, and C. Champion, Tilda-v: A full-differential code for proton tracking in biological matter, J. Phys. Conf. Ser. **635**, 032063 (2015).
[6] S. M. Pimblott and J. A. LaVerne, Production of low-energy electrons by ionizing radiation, Radiat. Phys. Chem. **76**, 1244 (2007).
[7] G. Baldacchino, Pulse radiolysis in water with heavy-ion beams. A short review, Radiat. Phys. Chem. **77**, 1218 (2008).
[8] V. Svoboda, R. Michiels, A. C. LaForge, J. Med, F. Stienkemeier, P. Slavicek, and H. J. Woerner, Real-time observation of water radiolysis and hydrated electron formation induced by extreme-ultraviolet pulses, Sci. Adv. **6**, eaaz0385 (2020).
[9] J. A. LaVerne, I. Stefanic, and S. M. Pimblott, Hydrated electron yields in the heavy ion radiolysis of water, J. Phys. Chem. A **109**, 9393 (2005).
[10] G. Baldacchino, G. Vigneron, J.-P. Renault, S. Pin, Z. Abedinzadeh, S. Deycard, E. Balanzat, S. Bouffard, M. Gardes-Albert, B. Hickel, and J.-C. Mialocq, A nanosecond pulse radiolysis study of the hydrated electron with high

energy ions with a narrow velocity distribution, Chem. Phys. Lett. **385**, 66 (2004).
[11] N. Saleh, K. Flippo, K. Nemoto, D. Umstadter, R. A. Crowell, C. D. Jonah, and A. D. Trifunac, Pulse radiolysis of liquid water using picosecond electron pulses produced by a table-top terawatt laser system, Rev. Sci. Instrum. **71**, 2305 (2000).
[12] Y. A. Gauduel, Y. Glinec, J.-P. Rousseau, F. Burgy, and V. Malka, High energy radiation femtochemistry of water molecules: early electron-radical pairs processes, Eur. Phys. J. D **60**, 121 (2010).
[13] Y. Muroya, M. Lin, Z. Han, Y. Kumagai, A. Sakumi, T. Ueda, and Y. Katsumura, Ultra-fast pulse radiolysis: A review of the recent system progress and its application to study on initial yields and solvation processes of solvated electrons in various kinds of alcohols, Radiat. Phys. Chem. **77**, 1176 (2008).
[14] D. A. Oulianov, R. A. Crowella, D. J. Gosztola, I. A. Shkrob, O. J. Korovyanko, and R. C. R. de Castro, Ultrafast pulse radiolysis using a terawatt laser wakefield accelerator, J. Appl. Phys. **101**, 053102 (2007).
[15] M. Borghesi, Laser-driven ion acceleration: State of the art and emerging mechanisms, Nucl. Instrum. Methods Phys. Res., Sect. A **740**, 6 (2014).
[16] B. Dromey, M. Coughlan, L. Senje, M. Taylor, S. Kuschel, B. Villagomez-Bernabe, R. Stefanuik, G. Nersisyan, L. Stella, J. Kohanoff, M. Borghesi, F. Currell, D. Riley, D. Jung, C.-G. Wahlstroem, C. L. S. Lewis, and M. Zepf, Picosecond metrology of laser-driven proton bursts, Nat. Commun. **7**, 10642 (2016).
[17] L. Senje, M. Coughlan, D. Jung, M. Taylor, G. Nersisyan, D. Riley, C. L. S. Lewis, O. Lundh, C. G. Wahlstrm, M. Zepf, and B. Dromey, Experimental investigation of picosecond dynamics following interactions between laser accelerated protons and water, Appl. Phys. Lett. **110**, 104102 (2017).
[18] A. M. Kellerer and D. Chmelevsky, Concepts of microdosimetry, Radiat. Environ. Biophys. **12**, 61 (1975).
[19] M. Roth and M. Schollmeier, Ion acceleration—target normal sheath acceleration, CERN Yellow Rep. **1**, 231 (2016).
[20] M. Passoni, L. Bertagna, and A. Zani, Target normal sheath acceleration: theory, comparison with experiments and future perspectives, New J. Phys. **12**, 045012 (2010).
[21] M. Coughlan, H. Donnelly, N. Breslin, C. Arthur, G. Nersisyan, M. Yeung, B. Villagomez-Bernabe, M. Afshari, F. Currell, M. Zepf, and B. Dromey, Ultrafast dynamics and evolution of ion-induced opacity in transparent dielectrics, New J. Phys. **22**, 103023 (2020).
[22] D. Polli, D. Brida, S. Mukamel, G. Lanzani, and G. Cerullo, Effective temporal resolution in pump-probe spectroscopy with strongly chirped pulses, Phys. Rev. A **82**, 053809 (2010).
[23] M. Pizzochero, F. Ambrosio, and A. Pasquarello, Picture of the wet electron: a localized transient state in liquid water, Chem. Sci. **10**, 7442 (2019).
[24] A. Hertwig, H. Hippler, and A. N. Unterreiner, Temperature-dependent studies of solvated electrons in liquid water with two and three femtosecond pulse sequences, Phys. Chem. Chem. Phys. **4**, 4412 (2002).
[25] K. R. Siefermann, Y. Liu, E. Lugovoy, O. Link, M. Faubel, U. Buck, B. Winter, and B. Abel, Binding energies, lifetimes and implications of bulk and interface solvated electrons in water, Nat. Chem. **2**, 274 (2010).
[26] B. Abel, U. Buck, A. L. Sobolewskic, and W. Domcke, On the nature and signatures of the solvated electron in water, Phys. Chem. Chem. Phys. **14**, 22 (2012).
[27] Y. Kimura, J. C. Alfano, P. K. Walhout, and P. F. Barbara, Ultrafast transient absorption spectroscopy of the solvated electron in water, J. Phys. Chem. **98**, 3450 (1994).
[28] L. Turi and P. J. Rossky, Theoretical studies of spectroscopy and dynamics of hydrated electrons, Chem. Rev. **112**, 5641 (2012).
[29] K. Yokoyama, C. Silva, D. H. Son, P. K. Walhout, and P. F. Barbara, Detailed investigation of the femtosecond pump-probe spectroscopy of the hydrated electron, J. Phys. Chem. **102**, 6957 (1998).
[30] F. Y. Jou and G. R. Freeman, Shapes of optical spectra of solvated electrons. Effect of pressure, J. Phys. Chem. **81**, 909 (1977).
[31] B. Rethfeld, A. Kaiser, M. Vicanek, and G. Simon, Femtosecond laser-induced heating of electron gas in aluminium, Appl. Phys. A **69**, S109 (1999).
[32] F. Bisesto, M. Galletti, M. P. Anania, G. Costa, M. Ferrario, F. Pompili, A. Zigler, F. Consoli, M. Cipriani, M. Salvadori, and C. Verona, Simultaneous observation of ultrafast electron and proton beams in tnsa, High Power Laser Sci. Eng. **8**, e23 (2020).
[33] J. Ma, U. Schmidhammer, and M. Mostafavi, Direct evidence for transient pair formation between a solvated electron and h3o+ observed by picosecond pulse radiolysis, J. Phys. Chem. Lett. **5**, 2219 (2014).
[34] M. Oncak, P. Slavicek, M. Farnik, and U. Buck, Photochemistry of hydrogen halides on water clusters: simulations of electronic spectra and photodynamics, and comparison with photodissociation experiments, J. Chem. Phys. A **115**, 6155 (2011).
[35] A. L. Sobolewski and W. Domcke, Hydrated hydronium: a cluster model of the solvated electron?, Phys. Chem. Chem. Phys. **4**, 4 (2002).
[36] M. Toulemonde, E. Surdutovich, and A. V. Solovyov, Temperature and pressure spikes in ion-beam cancer therapy, Phys. Rev. E **80**, 031913 (2009).
[37] *Ion Beam Modification of Solids*, edited by W. Wesch and E. Wendler (Springer, New York, 2016), Vol. 61.
[38] H. Schwoerer, S. Pfotenhauer, O. Jäckel, K.-U. Amthor, B. Liesfeld, W. Ziegler, R. Sauerbrey, K. W. D. Ledingham, and T. Esirkepov, Laserplasma acceleration of quasi-monoenergetic protons from microstructured targets, Nature (London) **439**, 445 (2006).
[39] B. M. Hegelich, B. J. Albright, K. F. J. Cobble, S. Letzring, M. Paffett, H. Ruhl, J. Schreiber, R. K. Schulze, and J. C. Fernandez, Laser acceleration of quasi-monoenergetic mev ion beams, Nature (London) **439**, 441 (2006).
[40] M. Schollmeier *et al.*, Controlled Transport and Focusing of Laser-Accelerated Protons with Miniature Magnetic Devices, Phys. Rev. Lett. **101**, 055004 (2008).

[41] T. Toncian, M. Borghesi, J. Fuchs, E. d'Humires, P. Antici, P. Audebert, E. Brambrink, C. A. Cecchetti, A. Pipahl, L. Romagnani, and O. Willi, Ultrafast laser-driven microlens to focus and energy-select mega-electron volt protons, Science **312**, 410 (2006).

[42] F. A. Cucinotta, F. K. Manuel, J. Jones, G. Iszard, J. Murrey, B. Djojonegro, and M. Wear, Space radiation and cataracts in astronauts, Radiat. Res. **156**, 460 (2001).

[43] M. Jermann, Particle therapy statistics in 2014, Int. J. Part. Ther. **2**, 50 (2015).

[44] U. Linz and J. Alonso, Laser-driven ion accelerators for tumor therapy revisited, Phys. Rev. Accel. Beams **19**, 124802 (2016).

[45] R. W. Hamm and M. E. Hamm, eds., *Industrial Accelerators and Their Applications* (World Scientific, Singapore, 2012).